LETTERS

Visualization of transient encounter complexes in protein–protein association

Chun Tang[1], Junji Iwahara[1] & G. Marius Clore[1]

Kinetic data on a number of protein–protein associations have provided evidence for the initial formation of a pre-equilibrium encounter complex that subsequently relaxes to the final stereospecific complex[1]. Site-directed mutagenesis[2–4] and brownian dynamics simulations[5–7] have suggested that the rate of association can be modulated by perturbations in charge distribution outside the direct interaction surfaces. Furthermore, rate enhancement through non-specific binding may occur by either a reduction in dimensionality[8] or the presence of a short-range, non-specific attractive potential[9]. Here, using paramagnetic relaxation enhancement, we directly demonstrate the existence and visualize the distribution of an ensemble of transient, non-specific encounter complexes under equilibrium conditions for a relatively weak protein–protein complex between the amino-terminal domain of enzyme I and the phosphocarrier protein HPr. Neither the stereospecific complex[10] alone nor any single alternative conformation can account fully for the intermolecular paramagnetic relaxation enhancement data. Restrained rigid-body simulated annealing refinement against the paramagnetic relaxation enhancement data enables us to obtain an atomic probability distribution map of the non-specific encounter complex ensemble that qualitatively correlates with the electrostatic surface potentials on the interacting proteins. Qualitatively similar results are presented for two other protein–protein complexes.

The association of the N-terminal domain of enzyme I (EIN) and the phosphocarrier protein HPr (dissociation constant, $K_d \approx 10\,\mu M$), the first binary complex in the bacterial phosphotransferase system[11], is in fast exchange on the chemical shift scale[10]. The structure of the stereospecific EIN–HPr complex has been solved by NMR on the basis of nuclear Overhauser enhancement (NOE) and residual dipolar coupling (RDC) data[10]. These data are fully consistent with a single, unique conformation that readily accounts for the phosphoryl transfer reaction between the two proteins[10]. However, neither the NOE nor the RDCs are sensitive to the presence of low-population (≤10%) intermediates. To detect such intermediates, we introduced a paramagnetic label at three sites on HPr, one at a time, and measured the transverse paramagnetic relaxation enhancement (PRE) rates, Γ_2, of the backbone amide protons (^1H_N) of EIN. In a fast exchanging system, the observed value of Γ_2 is the weighted average of the Γ_2 values for the various states present in solution[12,13]. Because Γ_2 is dependent on the sixth root of the distance ($<r^{-6}>$) between the unpaired electron on the paramagnetic centre and the observed proton, and because the Γ_2 rates at short distances are very large owing to the large magnetic moment of the unpaired electrons, low-population intermediates can be detected. Glu 5, Glu 25 and Glu 32 of HPr, which are all located outside the specific interaction surface with EIN, were substituted individually by a cysteine residue, which was then conjugated to EDTA through a disulphide linkage to yield a (cysteaminyl-EDTA)-Cys adduct. The latter is chelated to either Mn^{2+} (paramagnetic state) or Ca^{2+} (diamagnetic state)[14]. These modifications do not change the net charge of HPr, nor do they perturb the binding equilibrium with EIN.

The intramolecular ^1H_N-Γ_2 rates for HPr in the EIN–HPR complex are fully consistent with the static structure of HPr, with an overall PRE *Q*-factor[15] (for all three paramagnetic sites combined) of 0.18 and a correlation coefficient of 0.94 (Supplementary Fig. S1). (The *Q*-factor is a quantitative measure of agreement between observed and calculated Γ_2 rates and is given by equation (2) in the Methods section.) A comparison, however, of the observed intermolecular ^1H_N-Γ_2 rates measured on EIN with those back-calculated from the structure of the stereospecific complex as a function of residue number reveals regions with large discrepancies (Fig. 1). The correlation between observed and calculated intermolecular ^1H_N-Γ_2 rates is very poor, with an overall *Q*-factor of 0.61 (Fig. 2a). In the stereospecific complex, the intermolecular contacts predominantly involve helices α2 and α2′, the carboxy-terminal end of helix α3 and the N-terminal end of helix α4 of the α-domain of EIN, and helices α1 and α2 of HPr[10]. For each paramagnetic site, there are regions with large observed intermolecular ^1H_N-Γ_2 rates that are well predicted by the stereospecific complex (that is, they are in close proximity to the paramagnetic labels): namely, residues 110–137, 50–92 and 73–140 for Glu5→Cys, Glu25→Cys and Glu32→Cys, respectively, within the α-domain of EIN (Fig. 1). However, there are many other residues within the α-domain of EIN that are far away (≥25 Å) from the paramagnetic labels but show large ^1H_N-Γ_2 rates that are inconsistent with the structure of the specific complex: namely, residues 59–97, 105–124 and 20–71 for Glu5→Cys, Glu25→Cys and Glu32→Cys, respectively (Fig. 1). In addition, there are regions in the α/β domain, further away from the paramagnetic centres, where the agreement is poor to moderate: namely, residues 23–37, 183–189 and 241–249 for Glu25→Cys, and residues 184–189 and 232–249 for Glu32→Cys (Fig. 1). The discrepancies cannot be explained by a solvent PRE effect[16,17] involving diffusion and random collisions between EIN and the paramagnetically labelled HPr because, at the relatively low concentrations used (~300 μM), no significant PRE effects ($>2\,s^{-1}$) were observed for a control protein (that does not interact with HPr) on addition of paramagnetically labelled HPr. Thus, the observed intermolecular PRE data provide unambiguous qualitative evidence for the existence of lowly populated (≤10%) minor species in rapid exchange with the final stereospecific complex (see Supplementary Information).

A semi-quantitative depiction of the minor species was obtained by using restrained rigid-body simulated annealing refinement[18] to minimize the difference between observed and calculated ^1H_N-Γ_2 rates for all three paramagnetic sites simultaneously by representing the minor non-specific states by an ensemble of HPr molecules (with atomic overlap between HPr molecules allowed because the ensemble reflects a population distribution). We carried out 100 independent

[1]Laboratory of Chemical Physics, National Institute of Diabetes and Digestive and Kidney Diseases, National Institutes of Health, Bethesda, Maryland 20892-0520, USA.

calculations with ensemble sizes N ranging from 1 to 20, varying the percentage of the minor species (p_{minor}) relative to the stereospecific complex. Complete cross-validation[19], leaving out random portions of 10% of the complete PRE data set from all three sites, was done to assess how well the test PRE data sets (10% excluded from the refinement) are predicted by the working data sets (90% included in the refinement). Introduction of a single minor species results in only a modest decrease in the Q-factor, but, as the number of conformers is increased, a large decrease in the Q-factor is observed (Fig. 2c). Complete cross-validation indicates that the optimal number of conformers required to satisfy the data is 10–20 (Fig. 2c) and that the improvement in Q-factor is not a result of over-fitting the data. Thus, the minor species comprises many non-specific binding states that reflect an ensemble of transient encounter complexes.

The Q-factor decreases rapidly as p_{minor} is increased to 10% (Fig. 2d), a value that is still consistent with the NOE and RDC data, and thereafter slowly levels off. The Q-factor obtained by averaging the ^1H_N-Γ_2 rates over all ensembles (that is, the ensemble of ensembles average, Q_{ee}) is systematically smaller than the average Q-factor for the individual ensembles (Q_e). This is due to the stochastic rather than unique configuration of states within each ensemble, such that averaging over all ensembles affords a better representation of the data (Fig. 2c, d). For $N = 20$ and $p_{minor} = 10\%$, Q_{ee} has a value of 0.21 and the correlation coefficient between observed and calculated ^1H_N-Γ_2 rates is 0.97 (Fig. 2b), which is comparable to the agreement observed for the intramolecular PRE data (Supplementary Fig. S1). The overall population of minor non-specific encounter complexes may seem to be relatively high but is perhaps not unexpected for a relatively weak protein–protein association. However, the occupancy of any individual conformer in the ensemble of non-specific encounter complexes is very small and has therefore eluded structural characterization by any other experimental method.

The minor species were visualized by using a reweighted atomic probability density map[20] derived from 100 independent calculations using an ensemble size of $N = 20$ (Fig. 3a–c, left). The distribution of non-specifically bound HPr molecules on the surface of EIN is essentially continuous but non-uniform. The probability density in the region of the specific complex is low, indicating that alternative modes of binding confined to the contact surfaces involved in the stereospecific complex do not significantly contribute to the discrepancy between the observed PREs and those calculated on the basis of the specific complex (Supplementary Figs S2 and S3).

Outside the specific interaction surface, the distribution of HPr molecules (Fig. 3a–c, left) is qualitatively correlated with the negative electrostatic potential isosurface[21] of EIN (Fig. 3a–c, right). EIN is an acidic protein and large areas of its surface are swathed by a negative electrostatic potential. About half the surface of HPr, including the interaction surface used in the specific complex, is positively charged, and the remaining surface (formed predominantly by the β-sheet) is negatively charged. The HPr atomic probability density map heavily populates regions of EIN with highly negative electrostatic potentials, to a lesser extent around the C terminus of EIN, and minimally on the back of EIN (Supplementary Fig. S4a). Note that the HPr conformers located at the α/β domain are, on average, ~50 Å from HPr in the stereospecific complex. In all cases, HPr preferentially uses its positively charged surface to interact with the negatively charged regions of EIN (Supplementary Fig. S5c). Thus, the modifications used to introduce paramagnetic groups on HPr do not affect the formation of non-specific encounter complexes. These findings suggest that the formation of non-specific EIN–HPr encounter complexes is

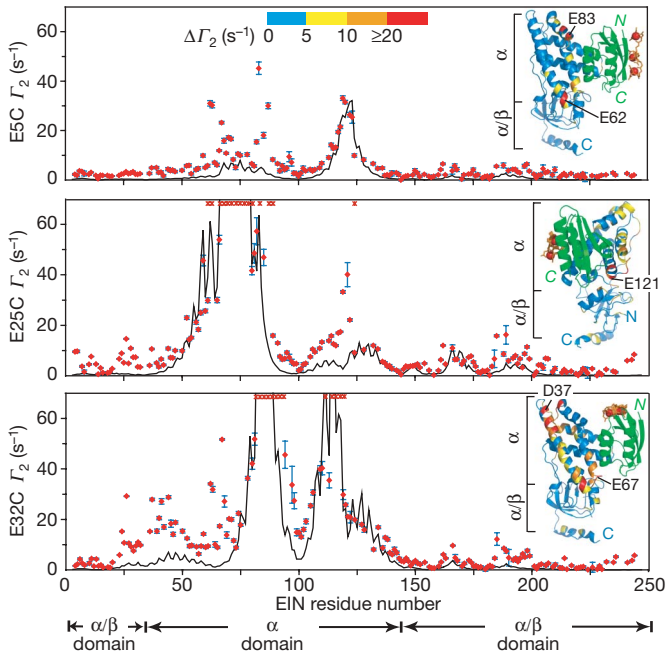

Figure 1 | Observed and calculated intermolecular PREs for the EIN–HPr complex. Shown is a comparison of observed intermolecular ^1H_N-Γ_2 rates (red diamonds) with those back-calculated (black lines) from the stereospecific complex; paramagnetic labels (EDTA-Mn^{2+}) were introduced one at a time at three sites (E5C, E25C and E32C) on HPr. Red crosses indicate residues with $^1H_N/^{15}N$ cross-peaks that are broadened beyond detection by PRE. Insets show the structure of the stereospecific EIN–HPr complex with EIN colour coded according to the difference, $\Delta\Gamma_2$, between the observed and calculated intermolecular ^1H_N-Γ_2 rates for each paramagnetic site. (HPr, green; three-member ensemble representation of EDTA-Mn^{2+} with EDTA and linkage, orange, and Mn^{2+}, red spheres).

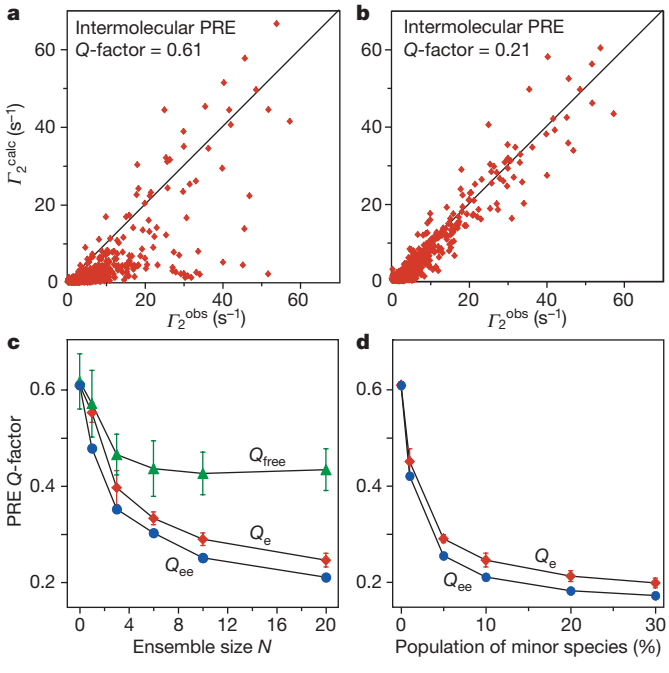

Figure 2 | Ensemble refinement and intermolecular PRE Q-factor. **a**, **b**, Correlation between observed intermolecular ^1H_N-Γ_2 rates (501 data points) and those calculated from the structure of the stereospecific complex either alone (**a**) or with the addition of an ensemble of $N = 20$ to represent the non-specific encounter complex (**b**; $p_{minor} = 10\%$; averaged over 100 independent calculations). **c**, Dependence of the working (Q_e, red; Q_{ee}, blue) and cross-validated (Q-free, green) Q-factors on ensemble size N ($p_{minor} = 10\%$). **d**, Dependence of Q_e and Q_{ee} on p_{minor} ($N = 20$). The points in **c** and **d** at $N = 0$ and $p_{minor} = 0$, respectively, represent control calculations in which $p_{minor} = 0$ and the position of HPr for the single specific complex is optimized by rigid-body simulated annealing to satisfy the intermolecular PRE data. Error bars indicate the s.d.

predominantly driven by weak non-specific electrostatic attractions between the two molecules.

The total solvent accessible surface area (ASA) buried at the interfaces of the non-specific encounter complexes is, on average, an order of magnitude smaller than that of the stereospecific complex (1,945 Å^2; Fig. 3d). The non-specific interfaces are also much less compact, with gap indices (defined as the ratio of gap volume to buried interface ASA[22]) many times larger than that of the stereospecific complex (2.1 Å; Fig. 3d). In addition, the non-specific interfaces are more planar than the stereospecific one, indicative of the absence of lock-and-key binding (Supplementary Table S1). These observations are consistent with the correlation between the spatial distribution of non-specific encounter complexes and electrostatic potential isosurface, because electrostatic interactions are relatively long range (with a $1/r$ distance dependence) and do not necessarily require van der Waals contact. The role of electrostatic interactions is reinforced by the observation that the interfacial composition of charged residues is increased, whereas that of uncharged polar and non-polar residues is decreased in the non-specific encounter complexes relative to the stereospecific complex (Supplementary Fig. S4b).

Once a non-specific encounter complex is formed by weak non-specific electrostatic interactions, HPr can carry out a two-dimensional search on the surface of EIN, eventually falling into a narrow energy funnel that leads directly to the stereospecific complex characterized by an array of complementary van der Waals and electrostatic interactions. The observation that the region on EIN comprising the specific interaction surface for HPr is only minimally occupied by non-specific encounter complexes (Fig. 3a) indicates that once HPr reaches this region formation of the stereospecific complex occurs with high probability.

The direct detection of non-specific encounter complexes by PRE is not confined to the EIN–HPr complex. We observed similar effects for two other weak ($K_d \approx 30$–$50\ \mu M$), fast-exchanging protein–protein complexes of the bacterial phosphotransferase system, IIA^{Mannitol}–HPr (Fig. 4) and IIA^{Mannose}–HPr (Supplementary Fig. S6), the stereospecific structures of which have been solved[23,24]. With the paramagnetic label on HPr located at Glu5→Cys, on the opposite face to the stereospecific binding site, there are regions in both complexes where the observed intermolecular ^1H_N-Γ_2 rates are much larger than those back-calculated from the structures of the stereospecific complexes. The largest discrepancies involve acidic residues of IIA^{Mannitol} and IIA^{Mannose}, the distribution of which correlates qualitatively with the negative electrostatic potential on the surface of these proteins. Thus, in all likelihood the observations

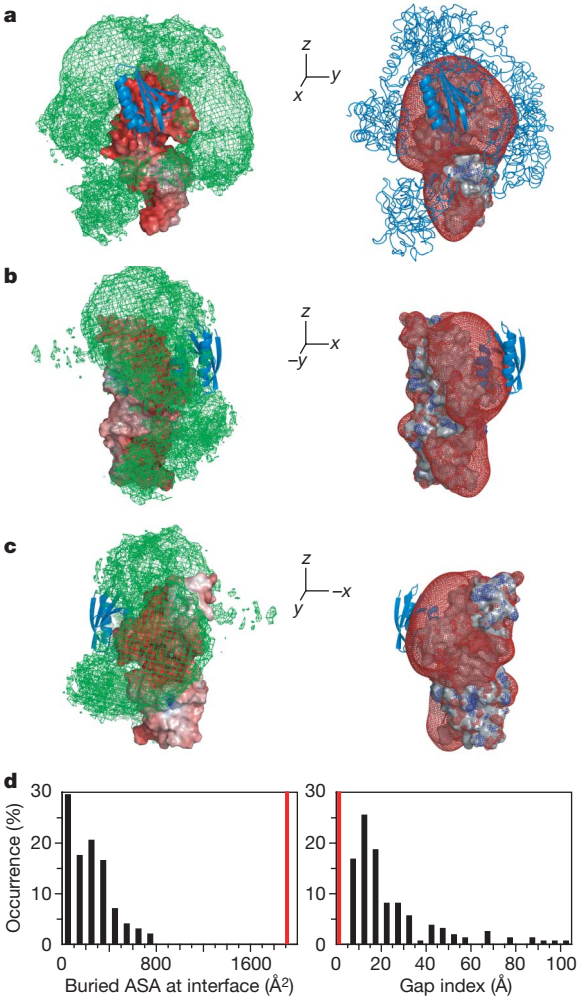

Figure 3 | Characterization of non-specific EIN–HPr encounter complexes. **a**–**c**, Left, overall distribution of HPr molecules obtained from 100 calculations ($N = 20$) displayed as a reweighted atomic probability density map[20] (plotted at a threshold of 20% maximum, green) on the molecular surface of EIN (colour coded by electrostatic potential, ±8 kT). Right, molecular surface of EIN in grey with the electrostatic potential isosurface of EIN, calculated at ±5 kT, displayed as red (negative) and blue (positive) meshes. The disposition of HPr molecules (blue tubes) in a typical ensemble of $N = 20$ is shown in the right panel of **a**. The location of HPr in the stereospecific complex is shown as a blue ribbon in all panels. **d**, Histograms of interface-buried ASA and gap index for the non-specific encounter complexes. Red lines indicate values for the stereospecific complex.

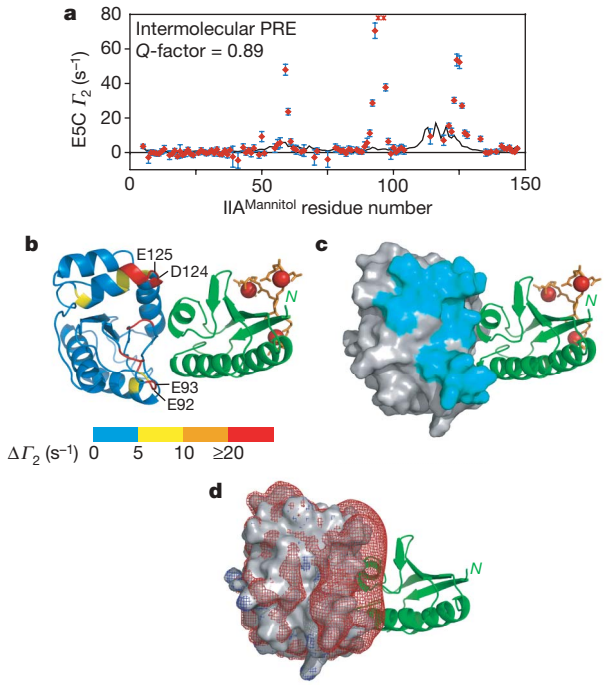

Figure 4 | Observed and calculated PRE ^1H_N-Γ_2 values for the IIA^{Mannitol}–HPr complex. EDTA-Mn^{2+} paramagnetic labels were introduced onto HPr at E5C. **a**, Comparison of observed intermolecular ^1H_N-Γ_2 rates (red diamonds) with those back-calculated (black lines) from the stereospecific complex. Red crosses indicate residues with $^1H_N/^{15}N$ cross-peaks that are broadened beyond detection by PRE; error bars indicate the s.d. **b**, Structure of the stereospecific complex with IIA^{Mannitol} colour coded according to the difference, $\Delta\Gamma_2$, between observed and calculated intermolecular ^1H_N-Γ_2 rates. Colouring for HPr and EDTA-Mn^{2+} as in Fig. 1 insets. **c**, Molecular surface representation of IIA^{Mannitol} in the stereospecific complex. Residues of IIA^{Mannitol} that show large $\Delta\Gamma_2$ are coloured cyan. **d**, Electrostatic potential isosurface of IIA^{Mannitol} (±5 kT in blue and red, respectively). In **c** and **d**, HPr is shown as a green ribbon. The same view is shown in **b**–**d**.

reported here reflect a general phenomenon of protein–protein association in which the initial formation of non-specific encounter complexes through long-range electrostatic interactions (possibly supplemented by short-range van der Waals interactions) facilitates the rapid formation of a stereospecific complex by reducing the dimensionality of the search process.

METHODS

Sample preparation and NMR spectroscopy. Details of sample preparation are provided in Supplementary Information. We acquired PRE data on a Bruker DRX-600 spectrometer as described[15] (see Supplementary Information).

Back-calculation of PREs. Intra- and intermolecular PREs were back-calculated from the structures of the stereospecific complexes by using a three-conformer ensemble representation for the EDTA-Mn^{2+} groups to account for their flexibility (see Supplementary Information)[15].

Ensemble refinement against intermolecular PREs. Refinement against the intermolecular PREs for the EIN–HPr complex was carried out by rigid body refinement with Xplor-NIH[18] subject to a target function comprising the PRE data for all three paramagnetic sites[15], a quartic van der Waals repulsion term[25] (to prevent atomic overlap between EIN and HPr) and a very weak radius of gyration restraint[26] (to ensure that each member of the ensemble makes at least some intermolecular contacts). Calculations were carried out either by keeping EIN fixed and allowing an ensemble of HPr molecules to rotate and translate, or by the converse (HPr fixed and an ensemble of EIN molecules), with essentially identical results (Supplementary Fig. S5). Further details of the calculations are provided in Supplementary Information. The calculated PRE for residue i, $\Gamma_2^{\mathrm{calc}}(i)$, is given by

$$\Gamma_2^{\mathrm{calc}}(i) = \lambda \Gamma_2^{\mathrm{specific}}(i) + (1-\lambda)\sum_{j=1}^{N} \Gamma_2^{\mathrm{non\text{-}specific}}(i,j)/N \qquad (1)$$

where λ is the fraction of the stereospecific complex ($\lambda = 1 - p_{\mathrm{minor}}$), N is the ensemble size of the non-specific encounter complex, $\Gamma_2^{\mathrm{specific}}(i)$ is the calculated Γ_2 rate for residue i in the stereospecific complex, and $\Gamma_2^{\mathrm{non\text{-}specific}}(i,j)$ is the calculated Γ_2 rate for residue i of member j of the non-specific encounter complex ensemble. The PRE Q-factor is a measure of the agreement between observed and calculated values of Γ_2 and is given by:

$$Q = \left[\sum_i \{\Gamma_2^{\mathrm{obs}}(i) - \Gamma_2^{\mathrm{calc}}(i)\}^2 / \sum_i \Gamma_2^{\mathrm{obs}}(i)^2\right]^{1/2} \qquad (2)$$

where $\Gamma_2^{\mathrm{obs}}(i)$ is the observed Γ_2 rate for residue i. Two Q-factors are reported: Q_e is the average Q-factor $<Q>$ for all calculated n ensembles, with $\Gamma_2^{\mathrm{calc}}(i)$ computed by equation (1); Q_{ee} is the ensemble of ensembles average Q-factor, computed by using the average value of $\Gamma_2^{\mathrm{calc}}(i)$ over all n ensembles, with $\Gamma_2^{\mathrm{calc}}(i)$ given by:

$$\Gamma_2^{\mathrm{calc}}(i) = \lambda \Gamma_2^{\mathrm{specific}}(i) + (1-\lambda)\sum_{k=1}^{n}\sum_{j=1}^{N} \Gamma_2^{\mathrm{non\text{-}specific}}(i,j,k)/nN \qquad (3)$$

Analysis of complexes. Electrostatic potentials were calculated with APBS[21] and are displayed in PyMol[27]. Solvent ASA buried at the interface and gap volume were calculated with Xplor-NIH[18] and SURFNET[28], respectively.

Received 23 May; accepted 4 September 2006.
Published online 15 October 2006.

1. Fersht, A. R. *Structure and Mechanism in Protein Science: a Guide to Enzyme Catalysis and Protein Folding* (Freeman & Co, New York, 1999).
2. Schreiber, G. & Fersht, A. R. Rapid electrostatically assisted association of proteins. *Nature Struct. Biol.* **3,** 427–431 (1996).
3. Vijaykumar, M. *et al.* Electrostatic enhancement of diffusion-controlled protein–protein association: comparison of theory and experiment on barnase and barstar. *J. Mol. Biol.* **278,** 1015–1024 (1998).
4. Selzer, T., Albeck, S. & Schreiber, G. Rational design of faster associating and tighter binding protein complexes. *Nature Struct. Biol.* **7,** 537–541 (2000).
5. Northrup, S. H., Boles, J. O. & Reynolds, J. C. L. Brownian dynamics of cytochrome c and cytochrome *c* peroxidase association. *Science* **241,** 67–70 (1988).
6. Gabdoulline, R. R. & Wade, R. C. Biomolecular diffusional association. *Curr. Opin. Struct. Biol.* **12,** 204–213 (2002).
7. Spaar, A., Dammer, C., Gabdoulline, R. R., Wade, R. C. & Helms, V. Diffusional encounter of barnase and barstar. *Biophys. J.* **90,** 1913–1924 (2006).
8. Adams, G. & Debruck, M. in *Structural Chemistry and Molecular Biology* (eds Rich, A. & Davidson, N.) 198–215 (Freeman & Co, San Francisco, CA, 1968).
9. Zhou, H-X. & Szabo, A. Enhancement of association rates by nonspecific binding to DNA and cell membranes. *Phys. Rev. Lett.* **93,** 178101 (2004).
10. Garrett, D. S., Seok, Y-J., Peterkofsky, A., Gronenborn, A. M. & Clore, G. M. Solution structure of the 40,000 M_r phosphoryl transfer complex between the N-terminal domain of enzyme I and HPr. *Nature Struct. Biol.* **6,** 166–173 (1999).
11. Postma, P. W., Lengeler, J. W. & Jacobson, G. R. in *Escherichia coli and Salmonella: Cellular and Molecular Biology* (ed. Neidhardt, F. C.) 1149–1174 (ASM, Washington DC, 1996).
12. Iwahara, J. & Clore, G. M. Detecting transient intermediates in macromolecular binding by paramagnetic NMR. *Nature* **440,** 1227–1230 (2006).
13. Iwahara, J., Schwieters, C. D. & Clore, G. M. Characterization of nonspecific protein–DNA interactions by ^{1}H paramagnetic relaxation enhancement. *J. Am. Chem. Soc.* **126,** 12800–12808 (2004).
14. Ebright, Y. W., Chen, Y., Pendergrast, P. S. & Ebright, R. H. Incorporation of an EDTA–metal complex at a rationally selected site within a protein: application to EDTA–iron DNA affinity cleaving with catabolite gene activator protein (CAP) and Cro. *Biochemistry* **31,** 10664–10670 (1992).
15. Iwahara, J., Schwieters, C. D. & Clore, G. M. Ensemble approach for NMR structure refinement against ^{1}H paramagnetic relaxation enhancement data arising from a flexible paramagnetic group attached to a macromolecules. *J. Am. Chem. Soc.* **126,** 5879–5896 (2004).
16. Donaldson, L. W. *et al.* Structural characterization of proteins with an attached ATCUN motif by paramagnetic relaxation enhancement NMR spectroscopy. *J. Am. Chem. Soc.* **123,** 9843–9847 (2001).
17. Pintacuda, G. & Otting, G. Identification of protein surfaces by NMR measurements with a paramagnetic Gd(III) chelate. *J. Am. Chem. Soc.* **124,** 372–373 (2002).
18. Schwieters, C. D., Kuszewski, J. J. & Clore, G. M. Using Xplor-NIH for NMR molecular structure determination. *Prog. NMR Spectrosc.* **48,** 47–62 (2006).
19. Brünger, A. T., Clore, G. M., Gronenborn, A. M. & Nilges, M. Assessing the quality of solution nuclear magnetic resonance structures by complete cross-validation. *Science* **261,** 328–331 (1993).
20. Schwieters, C. D. & Clore, G. M. Reweighted atomic densities to represent ensembles of NMR structures. *J. Biomol. NMR* **23,** 221–225 (2002).
21. Baker, N. A., Sept, D., Joseph, S., Holst, M. J. & McCammon, J. A. Electrostatics of nanosystems: application to microtubules and the ribosome. *Proc. Natl Acad. Sci. USA* **98,** 10037–10041 (2001).
22. Jones, S. & Thornton, J. M. principles of protein–protein interactions. *Proc. Natl Acad. Sci. USA* **93,** 13–20 (1996).
23. Cornilescu, G. *et al.* Solution structure of the phosphoryl transfer complex between the cytoplasmic A domain of the mannitol transporter $II^{Mannitol}$ and HPr of the *Eschrichia coli* phosphotransferase system. *J. Biol. Chem.* **277,** 42289–42298 (2002).
24. Williams, D. C., Cai, M., Suh, Y-J., Peterkofsky, A. & Clore, G. M. Solution NMR structure of the 48 kDa $IIA^{Mannose}$–HPr complex of the *Escherichia coli* mannose phosphotransferase system. *J. Biol. Chem.* **280,** 20775–20784 (2005).
25. Nilges, M., Gronenborn, A. M., Brünger, A. T. & Clore, G. M. Determination of three-dimensional structures of proteins by simulated annealing with interproton distance restraints: application to crambin, potato carboxypeptidase inhibitor and barley serine proteinase inhibitor 2. *Protein Eng.* **2,** 27–38 (1988).
26. Kuszewski, J., Gronenborn, A. M. & Clore, G. M. Improving the packing and accuracy of NMR structures with a pseudopotential for the radius of gyration. *J. Am. Chem. Soc.* **121,** 2337–2338 (1999).
27. DeLano, W. L. The PyMOL Molecular Graphics System (DeLano Scientific, San Carlos, CA, USA, 2002).
28. Laskowski, R. A. SURFNET: a program for visualizing molecular surfaces, cavities and intermolecular interactions. *J. Mol. Graph.* **13,** 323–330 (1995).

Supplementary Information is linked to the online version of the paper at www.nature.com/nature.

Acknowledgements We thank C. Schwieters, A. Szabo and C. Bewley for discussions; and C. Byeon for assistance with initial sample preparation. This work was supported by funds from the Intramural Program of the NIH, NIDDK and the AIDS Targeted Antiviral program of the Office of the Director of the NIH (to G.M.C.).

Author Information Reprints and permissions information is available at www.nature.com/reprints. The authors declare no competing financial interests. Correspondence and requests for materials should be addressed to G.M.C. (mariusc@intra.niddk.nih.gov).